

# Electrochemical Fluoridation of Manganese Oxide by Perfluorinated-Gas Conversion for Lithium-Ion Cathodes

Haining Gao,<sup>[a]</sup> Mingfu He,<sup>[b]</sup> Rui Guo,<sup>[b]</sup> and Betar M. Gallant<sup>\*[b]</sup>

Fluoridation of Lithium-ion (Li-ion) cathodes is of growing interest for high-capacity  $\text{Li}^+$  storage materials, but well-controlled fluoridation processes are elusive. We investigated an electrochemical methodology to grow lithium fluoride (LiF) by reduction of perfluorinated gas onto metal oxides (MO), which then forms M–O–F by splitting of LiF upon charge, using MnO as an example target phase. Unlike current methods where particle size  $<10\text{ nm}$  is necessary for high MnO utilization (subsequent discharge/lithiation capacity), owing to

the nano-crystallinity and intimate contact of electrochemically-grown LiF, high MnO utilization ( $\sim 0.9 \text{ e}^-/\text{MnO}$ ,  $340 \text{ mAh g}_{\text{MnO}}^{-1}$ ) is achieved with large MnO particle size ( $\sim 400 \text{ nm}$ ), exceeding comparable MnO/LiF systems reported to date. Additionally, incorporation of perfluorinated-gas additive benefits cycling, with capacity of  $\sim 270 \text{ mAh g}_{\text{MnO}}^{-1}$  retained after 20 cycles. This work demonstrates the opportunity for electrochemically driven fluoridation to achieve high capacities with larger particle sizes needed to bring oxyfluorides closer to practical reality.

## 1. Introduction

Sustained demand for higher-energy rechargeable Li/Li-ion batteries that can reach U.S. Department of Energy targets of  $500 \text{ Wh kg}^{-1}$  and  $750 \text{ Wh L}^{-1}$  motivates continued improvement beyond today's cathode materials, which limit cell performance.<sup>[1]</sup> Commercialized Li-ion battery cathodes belong mainly to oxide-based materials, with current focus on lithium nickel-manganese-cobalt oxide (NMC) with capacities of  $\sim 200 \text{ mAh g}^{-1}$ .<sup>[2]</sup> Many oxides currently under development that can attain higher capacities, such as Li-rich cathodes (e.g. Li-rich NMC,  $> 280 \text{ mAh g}^{-1}$ )<sup>[3]</sup> or Li-rich disordered rock-salt phases ( $> 300 \text{ mAh g}^{-1}$ ),<sup>[4]</sup> rely on anionic redox, which triggers oxygen release along with transition metal dissolution during cycling, plaguing cell stability.<sup>[5]</sup> In this context, there has been great interest in identifying strategies to improve cyclability of oxide parent phases, of which fluorination/fluoridation methods have received focus in recent years.<sup>[6]</sup> The high electronegativity of fluorine (F) and exceptionally high free energy of formation of fluorides imparts strong metal-F bonds,<sup>[7]</sup> stabilizing transition metal species from migration and improving lattice stability. Bulk-phase F-substitution for oxygen (O) has so far been conducted in oxides with various structures (spinel  $\text{LiMn}_2\text{O}_4$ , layered NMC, and Nb-based disordered rock-salt), yielding improved cyclability, higher discharge voltage, and increased capacity.<sup>[6a–f]</sup> In addition to bulk substitution, surface F-modification, such as nanoscopic LiF coatings, can protect

the oxides against the electrolyte under highly oxidizing conditions, helping to suppress side reactions while sustaining prolonged cycle life.<sup>[6g]</sup>

More recently, LiF surface modification has been reported to support bulk-like fluoridation of oxide phases upon electrochemical activation at high potentials. Kang and co-workers, using composites composed of LiF and non-lithiated transition metal oxides synthesized by high energy ball milling, demonstrated that the initial charge step induces an LiF “splitting” (activation) reaction<sup>[8]</sup> upon oxidation of a nearby transition metal site, viz Equation (1):



where M=Mn, Fe, or Co. When used with a non-Li-containing oxide like the monoxide class MO, LiF acts as both an F and a Li source, with  $\text{Li}^+$  migration to the anode as  $\text{F}^-$  is incorporated into the cathode to balance oxidation of M, and thus has an additional benefit of providing Li to the cathode and cell. Following activation, the resulting M–O–F phase, which reportedly has a disordered structure with an F-rich amorphous shell and an O-rich core, then cycles as a conversion cathode with reversible capacities up to  $240 \text{ mAh g}_{\text{MnO+LiF}}^{-1}$  (or  $\sim 345 \text{ mAh g}_{\text{MnO}}^{-1}$ ). Achieving these capacities previously required very small oxide/LiF particle sizes ( $< 10 \text{ nm}$  for MO), which were reported as necessary to achieve meaningful degrees of fluoridation. This occurs because, upon first charge, F largely concentrates in the MnO surface region; consequently, large surface areas are needed to facilitate high MnO utilization.<sup>[8b,9]</sup> In contrast to mechanical milling, Tarascon and co-workers proposed a distinct approach for *in situ* fluoridation of oxides through  $\text{LiPF}_6$  salt decomposition, attaining a capacity of  $\sim 250 \text{ mAh g}_{\text{MnO}}^{-1}$ .<sup>[10]</sup> However, the decomposition of salt demands excess electrolyte and will inevitably lead to other parasitic reactions. Finally, thin-film methods, such as pulse laser deposition (PLD), have recently been explored to form LiF/Fe/Cu or LiF/NiFe<sub>2</sub>O<sub>4</sub> films with small domain sizes for both

[a] H. Gao

*Department of Materials Science and Engineering  
Massachusetts Institute of Technology*

*77 Massachusetts Avenue, Cambridge, Massachusetts 02139, United States*

[b] Dr. M. He, R. Guo, Prof. B. M. Gallant

*Department of Mechanical Engineering  
Massachusetts Institute of Technology  
77 Massachusetts Avenue, Cambridge, Massachusetts 02139, United States  
E-mail: bgallant@mit.edu*

 Supporting information for this article is available on the WWW under <https://doi.org/10.1002/batt.202100139>

LiF and M/MO phases (<10 nm) and improved contact between LiF and transition metal species.<sup>[11]</sup> Scalability of the thin film processing methods requires further development. Consequently, methodologies of F incorporation need further exploration and improvement to broaden applicability to practical battery materials, especially where high tap densities require larger particle sizes (up to several  $\mu\text{m}$ )<sup>[12]</sup> and where parasitic salt consumption is untenable.

We hypothesized, given extensive reliance on ball-milling in previous work and known difficulty in LiF processing to form well-controlled interfaces, that poor physical/electrical contact between the MO substrate and LiF could limit attainable degrees of fluoridation below what may be achievable, contributing to stringent particle-size requirements seen previously. To test this hypothesis, and to examine another possible fluoridation methodology with potential to help elucidate the limitations of those used so far, this study investigated whether higher degrees of fluoridation, as evidenced by higher discharge capacities, are achievable using an electrochemically sourced LiF formed by reduction of perfluorinated gases. Recently, we have found that the full reduction of SF<sub>6</sub> ( $\text{SF}_6 + 8\text{e}^- + 8\text{Li}^+ \rightarrow \text{Li}_2\text{S} + 6\text{LiF}$ )<sup>[13]</sup> and NF<sub>3</sub> ( $\text{NF}_3 + 3\text{e}^- + 3\text{Li}^+ \rightarrow 3\text{LiF} + \frac{1}{2}\text{N}_2$ )<sup>[14]</sup> occurs on carbon cathodes at potentials of 2–3 V vs. Li/Li<sup>+</sup>, thus the gases act as a highly-F-dense and electroactive molecular LiF source. Moreover, the morphology of the electrochemically formed LiF, which nucleates and grows as nanoscale particles (with diameters ranging from 20 nm to >400 nm) on the cathode substrate, was found to be highly versatile and could be tailored by modulating conditions such as electrolyte, discharge rate, and capacity. Herein, we examine the electrochemical nucleation and growth of LiF from these perfluorinated gases to form an intimate coating on an electronically conductive oxide for the first time (Figure 1). Owing to the good contact with MnO and the nano-crystallinity of LiF, we find that the electrochemically formed, LiF-coated MnO exhibits higher utilization (~0.9 e<sup>-</sup>/MnO) with larger particles (~400 nm), consistent with a higher degree of fluoridation, compared to the ball-milled composites (~40 nm,

<0.7 e<sup>-</sup>/MnO) and those fluoridated from salt-based reactions previously reported with similar particle sizes (~0.6 e<sup>-</sup>/MnO).<sup>[10]</sup>

## 2. Results and Discussion

### 2.1. Electrochemical Formation and Characterization of LiF Coating on MnO

MnO was chosen as a model substrate for fluorination in this work because it has been used in prior LiF splitting studies,<sup>[8b,10]</sup> providing sufficient data for comparison across methodologies, whereas few reports have investigated pre-lithiated Mn-containing compounds. The understanding gained from this study is expected to help with developing fluorinated practical oxide cathodes both without and with intrinsic Li sites. Due to the large particle size of the as-received MnO (~0.25 mm), a short ball-mill of 3 h was conducted on MnO/Vulcan carbon (VC, ~50 nm) mixture (MnO:VC = 7:2 w/w) to reduce the particle size to  $\sim 400 \pm 300$  nm (Figure S1). The resulting powder was then mixed with VC and polyvinylidene fluoride (PVDF) binder to form cathode materials (with a weight ratio of MnO:VC: PVDF = 55:35:10) and was coated onto Toray paper (5 wt% Teflon treated). In this work, 0.1 M lithium perchlorate (LiClO<sub>4</sub>) was used as the salt to eliminate additional F sources in the electrolyte other than the fluorinated gas. For the first discharge (LiF formation step), tetraethylene glycol dimethyl ether (TEGDME) was used as the solvent given its ability to promote more film-like LiF upon SF<sub>6</sub> reduction (typical LiF particle sizes of ~30 nm with conformal coating on carbon) with better electrical contact with the underlying substrate, as opposed to larger discrete LiF particles (~100 nm) with exposed carbon surfaces as observed with higher-donor-number solvents like DMSO.<sup>[13b]</sup> In addition, SF<sub>6</sub> exhibits higher discharge capacity in ethers than in carbonate solvents<sup>[13b]</sup> allowing more versatility for tailoring and studying electrochemically-formed LiF on MnO. Swagelok-type cells were assembled with Li anodes, the indicated cathode and electro-

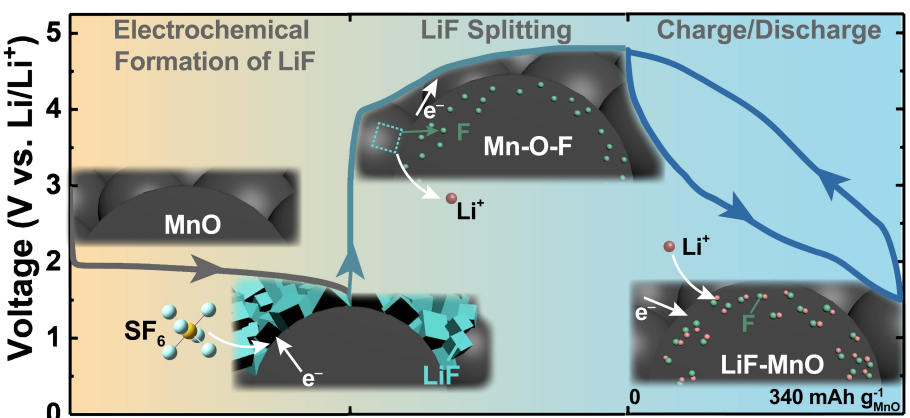


**Figure 1.** Schematic depicting electrochemical fluoridation of MnO cathodes using SF<sub>6</sub> gas as an exemplar fluorination source. Step 1: Electrochemical nucleation and growth of LiF occurs on MnO upon cathodic SF<sub>6</sub> reduction. Step 2: MnO/LiF electrodes are charged to induce electrochemical splitting of LiF and concurrent MnO fluoridation; as depicted, this process initiates at the surface of MnO particles and can continue into the bulk as charging proceeds. Step 3: Subsequent cycling occurs between the nominal end phases Mn–O–F↔LiF–MnO.

lyte, and were purged with  $\text{SF}_6$  or  $\text{NF}_3$ , pressurized to ~1 bar (typical gas solubilities ~1–5 mM)<sup>[13a,14]</sup> and sealed for testing.

Typical first-discharge profiles under galvanostatic conditions are shown in Figure 2(a). Without any fluorinated gas,  $\text{MnO}$  electrodes exhibited negligible capacity upon discharge (~30 mAh g<sub>MnO</sub><sup>-1</sup>) as expected for  $\text{Mn}^{2+}$  which is inactive in this voltage window.<sup>[15]</sup> In contrast, cells containing fluorinated gas exhibited electrochemical activity corresponding to gas reduction. The discharge potential of  $\text{NF}_3$ -containing cells (~2.1 V) at 75 mA g<sub>C</sub><sup>-1</sup> (~48 mA g<sub>MnO</sub><sup>-1</sup>) was similar to that on VC cathodes as measured previously,<sup>[14]</sup> indicating that the inclusion of  $\text{MnO}$  does not significantly affect the reduction behavior of  $\text{NF}_3$ . Typical discharge capacities of Li-NF<sub>3</sub> cells on MnO/VC cathodes are 1100 mAh g<sub>MnO</sub><sup>-1</sup> (~1700 mAh g<sub>C</sub><sup>-1</sup>), corresponding to an  $\text{NF}_3$  (consumed, assuming 3 e<sup>-</sup> transfer per  $\text{NF}_3$  molecule) to MnO molar ratio of 1:1. X-ray diffraction (XRD) in Figure 2(b) shows that LiF is the only crystalline phase formed following  $\text{NF}_3$  reduction. From scanning electron microscopy (SEM), a LiF layer was observed which covers the composite cathode, including the MnO particles, uniformly (Figure 2c).

In comparison, discharge of MnO/VC electrodes with  $\text{SF}_6$  gas at 100 mA g<sub>C</sub><sup>-1</sup> (~65 mA g<sub>MnO</sub><sup>-1</sup>) occurred ~100 mV below  $\text{NF}_3$  throughout discharge, which is similar to previous discharge voltages of  $\text{SF}_6$  on VC electrodes in TEGDME.<sup>[13b]</sup> Typical discharge capacities for  $\text{SF}_6$  cells with MnO/VC electrodes are 900 mAh g<sub>MnO</sub><sup>-1</sup> (~1400 mAh g<sub>C</sub><sup>-1</sup>), corresponding to a  $\text{SF}_6$  (consumed, assuming 8 e<sup>-</sup> transfer per  $\text{SF}_6$  molecule) to MnO molar ratio of 0.3:1. In contrast to reduction of  $\text{NF}_3$ , only very broad and weak LiF diffraction peaks were detected by

XRD after reduction of  $\text{SF}_6$  (Figure 2b), which indicates a substantially lower crystallinity and smaller particle sizes for the discharge product. Instead, X-ray photoelectron spectroscopy (XPS) was used to identify the composition of the formed phases. From the F 1s high-resolution scan (Figure 2d), a strong LiF peak at 684.9 eV was observed.<sup>[16]</sup> The existence of LiF was further confirmed from liquid <sup>19</sup>F nuclear magnetic resonance (NMR) spectroscopy (Figure S2) upon reacting discharged cathodes with water (D<sub>2</sub>O) to solubilize the LiF, which yielded a strong peak at ~122 ppm attributed to LiF.<sup>[17]</sup> A negligible amount of S was detected in the discharged cathode from XPS (Figure S3). This is consistent with previous results that showed a tendency of reduced-S phases such as polysulfides to solubilize in the electrolyte upon discharge during  $\text{SF}_6$  reduction. Therefore, both cathodes are predominantly LiF-coated MnO with differing degrees of LiF crystallinity. From the SEM image in Figure 2(c), the LiF layer formed using  $\text{SF}_6$  was similarly uniform and conformal.

## 2.2. LiF Splitting, MnO Fluoridation and Subsequent Lithiation

The MnO activation (charge) process was next investigated using 1 M LiClO<sub>4</sub> in ethylene carbonate and dimethyl carbonate (EC/DMC, v:v = 1:1) as electrolyte, which is more amenable to tolerate the high potentials required upon subsequent charging and LiF splitting when MnO is the substrate. Cells consisted of fresh Li anodes and MnO-containing cathodes, e.g.,

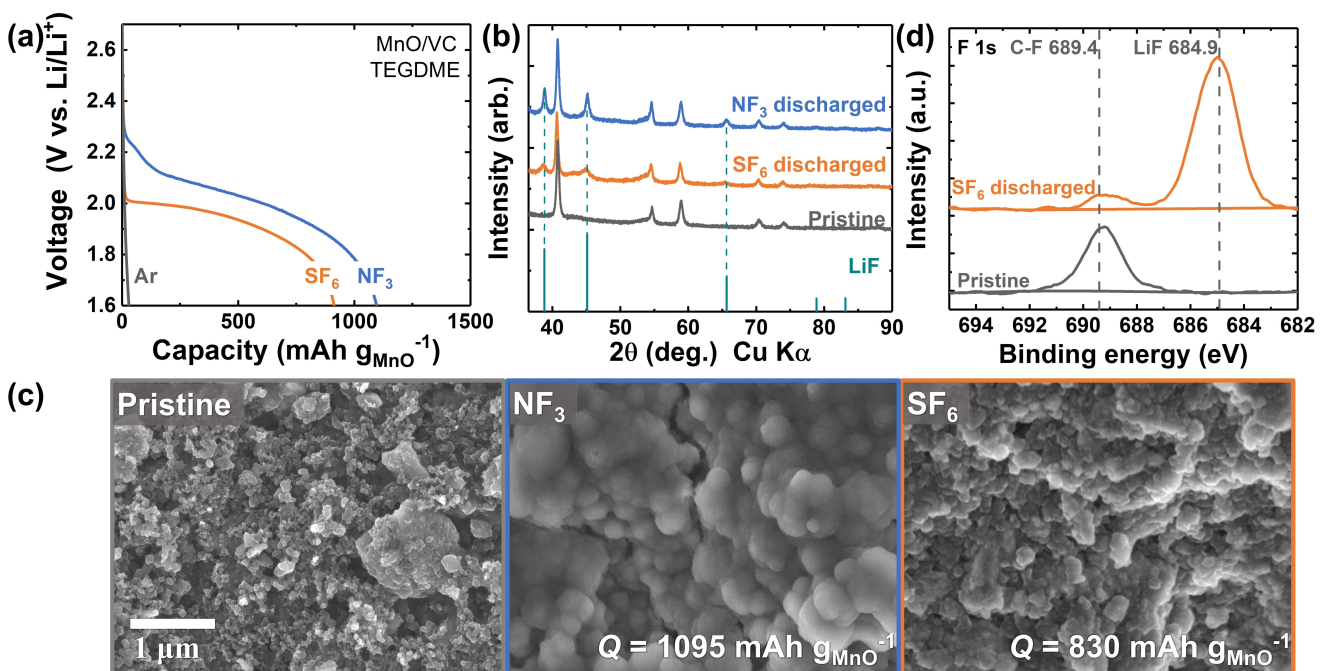


**Figure 2.** a) Galvanostatic discharge profiles of Li-SF<sub>6</sub> and Li-NF<sub>3</sub> cells using MnO/VC cathodes as the substrate at 100 mA g<sub>C</sub><sup>-1</sup> (~65 mA g<sub>MnO</sub><sup>-1</sup>) and 75 mA g<sub>C</sub><sup>-1</sup> (~48 mA g<sub>MnO</sub><sup>-1</sup>), respectively. b) X-ray diffraction of a discharged electrode in the Li-NF<sub>3</sub> ( $Q = 1180 \text{ mAh g}_{\text{MnO}}^{-1}$ ) and Li-SF<sub>6</sub> ( $Q = 830 \text{ mAh g}_{\text{MnO}}^{-1}$ ) cells. c) SEM images of pristine electrodes and of electrodes discharged to full capacity using fluorinated gas as indicated. d) High-resolution F 1s XPS spectra of the discharged electrode of a Li-SF<sub>6</sub> cell. To avoid binder-induced F signal, a non-fluorinated binder, polyacrylonitrile (PAN), was used in the cathode instead of PVDF, thus the capacity (~310 mAh g<sub>MnO</sub><sup>-1</sup>) is lower than in a) for this particular cell. The C-F peak at 699.4 eV is from Toray paper.

previously discharged MnO/VC cathodes under  $\text{NF}_3$  or  $\text{SF}_6$ . In these first experiments, the re-assembled cells in carbonate electrolyte contained no fluorinated gas. Except where otherwise noted, the first charge of the MnO, with or without LiF present, consisted of a constant current (CC) process at  $20 \text{ mA g}_{\text{MnO}}^{-1}$  ( $\sim 0.05 \text{ C}$ ) to a cutoff of  $4.8 \text{ V}$  vs.  $\text{Li}/\text{Li}^+$ , followed by a constant voltage (CV) hold until the current decreased below  $10 \text{ mA g}_{\text{MnO}}^{-1}$ <sup>[8b,10a]</sup>. Henceforth, discharge rates are normalized to the weight of MnO instead of carbon as Mn

redox is the major contributor of reversible capacity. The theoretical capacity of Mn–O–F, assuming  $\text{Mn}^{2+}/\text{Mn}^{3+}$  redox, is  $378 \text{ mAh g}_{\text{MnO}}^{-1}$ . For MnO/VC without LiF, the charge capacity was limited ( $101 \text{ mAh g}_{\text{MnO}}^{-1}$ , Figure 3a) and reflected only capacitive-like behavior, likely dominated by the carbon particles (i.e., no voltage plateau was observed). During the following discharge, small capacity of  $< 80 \text{ mAh g}_{\text{MnO}}^{-1}$  was observed, which is  $\sim 2\times$  of that observed before with Ar discharge (Figure 2a) given the larger voltage window ( $\sim 2\times$ ,

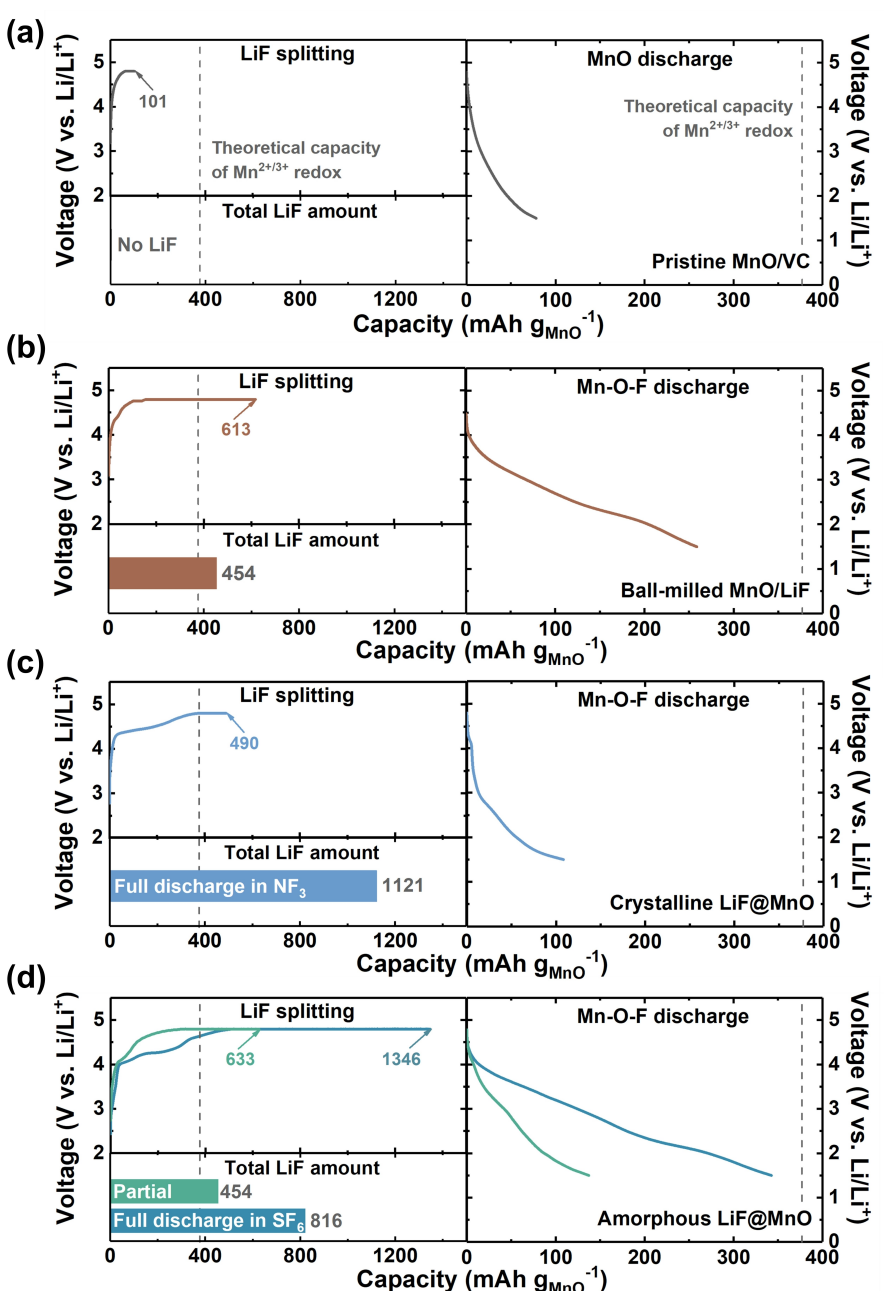


**Figure 3.** Electrochemical profiles of the first charge (LiF splitting) and the subsequent first discharge of the a) pristine MnO, b) ball-milled MnO/LiF, c) LiF@MnO (from fully discharged Li-NF<sub>3</sub> cells), and d) LiF@MnO (from partially and fully discharged Li-SF<sub>6</sub> cells) with 1 M LiClO<sub>4</sub> EC/DMC electrolyte. All the cells were CC charged at  $20 \text{ mA g}_{\text{MnO}}^{-1}$  ( $\sim 0.05 \text{ C}$ ) to  $4.8 \text{ V}$ , then CV charged with a cutoff of  $10 \text{ mA g}_{\text{MnO}}^{-1}$ , then CC discharged at  $20 \text{ mA g}_{\text{MnO}}^{-1}$  to  $1.5 \text{ V}$ . All three cathodes consist of 35 wt% of VC. The total LiF amount relative to MnO are indicated in each panel, which was calculated based on either the LiF added (for ball-milled sample in part b, assuming  $1 \text{ e}^-/\text{LiF}$ ), or the discharge capacity of Li-SF<sub>6</sub> or NF<sub>3</sub> cell (for part c and d). For the latter, each electron was assumed to produce 1 LiF for NF<sub>3</sub>, or  $6/8$  LiF for SF<sub>6</sub>. The theoretical capacity of MnO assuming Mn<sup>2+/3+</sup> redox,  $378 \text{ mAh g}_{\text{MnO}}^{-1}$ , is indicated as a grey dashed line.

4.8–1.5 V vs. ~3.1–1.6 V). This indicates no significant change to the MnO phase, which remained electrochemically inactive.

A mechanically ball milled MnO/LiF composite was prepared for comparison, with an MnO/LiF molar ratio of 1:1.2 with 20% LiF excess, and 20 wt% of VC, comparable to that used previously.<sup>[8b]</sup> The average particle size of the obtained MnO/LiF is  $\sim 40 \pm 25$  nm as measured from SEM (Figure S1), substantially smaller than that used for electrochemical fluoridation used herein. Given the amount of LiF present in the as-prepared ball-milled cathode, full splitting of LiF would correspond to a capacity of  $454 \text{ mAh g}_{\text{MnO}}^{-1}$ , which is higher than the theoretical capacity of MnO ( $378 \text{ mAh g}_{\text{MnO}}^{-1}$ ) owing to excess LiF. Experimentally, an initial charge capacity even higher, at  $613 \text{ mAh g}_{\text{MnO}}^{-1}$ , was observed (Figure 3b). Excess charge capacity beyond that used to fluorinate MnO is attributed to a combination of capacitive contributions and possibly to side reactions such as electrolyte oxidation, fluorination, or carbon oxidation.<sup>[18]</sup> We note that a capacity higher than the theoretical does not imply full conversion of MnO to MnOF. The following discharge/lithiation of the ball-milled MnO/LiF system exhibits a higher capacity of  $259 \text{ mAh g}_{\text{MnO}}^{-1}$  than that of pristine MnO/VC without LiF, proving successful activation of MnO to the Mn–O–F phase which then serves as a conversion Li-ion cathode. However, the lower capacity compared to the theoretical ( $378 \text{ mAh g}_{\text{MnO}}^{-1}$ ) confirms the fact that not all MnO was accessed by fluoridation in this system. The lower capacity than reported elsewhere for ball-milled samples ( $\sim 345 \text{ mAh g}_{\text{MnO}}^{-1}$ ) is attributed to the larger particle size ( $\sim 40 \pm 25$  nm) used here, vs. 8 nm in literature, since the fluoridation process is mainly surface-controlled and increased particle size reduces the total active surface area for F incorporation.<sup>[8b,9]</sup>

Electrochemically LiF-coated MnO cathodes (henceforth ‘LiF@MnO’) formed from SF<sub>6</sub> or NF<sub>3</sub> reduction were next compared. For LiF@MnO formed in a fully discharged Li-NF<sub>3</sub> cell (Figure 3c), a relatively limited charge (LiF splitting) capacity of  $490 \text{ mAh g}_{\text{MnO}}^{-1}$  was observed despite the large amount of LiF ( $> 1100 \text{ mAh g}_{\text{MnO}}^{-1}$  or  $1.9 \times$  excess), implying that not all LiF was electronically or electrochemically accessible for subsequent splitting. As a result, only limited capacity ( $108 \text{ mAh g}_{\text{MnO}}^{-1}$ ) was delivered during the subsequent discharge/lithiation of Mn–O–F, reflecting a low degree of MnO fluoridation/activation. The insufficient LiF splitting and MnO activation may be attributed to the large particle size of the crystallized LiF formed. Next, to form similar amount of LiF as that in the ball-milled MnO/LiF system, an SF<sub>6</sub> cell was partially discharged to a LiF amount equivalent to  $454 \text{ mAh g}_{\text{MnO}}^{-1}$ . The obtained LiF@MnO yielded a similar capacity upon charge/activation ( $633 \text{ mAh g}_{\text{MnO}}^{-1}$ ) as that for ball-milled MnO/LiF (Figure 3d), indicating that the charge capacity is proportional to the total LiF quantity. The subsequent discharge/lithiation capacity of this LiF@MnO from the partially discharged SF<sub>6</sub> cell was, however, only  $137 \text{ mAh g}_{\text{MnO}}^{-1}$ . We hypothesize that this low lithiation capacity is caused by the low degree of coating of MnO by LiF, recalling that LiF forms both on MnO and on VC (with the latter not contributing to reversible capacity) as was further supported by SEM images (Figure S4). Thus, to test this

hypothesis, LiF@MnO electrodes were formed with even higher LiF amounts by discharging Li-SF<sub>6</sub> cells to completion. As is shown in Figure 3(d), a larger capacity ( $> 1300 \text{ mAh g}_{\text{MnO}}^{-1}$ ) was attained from the first charge of the higher-LiF-loading LiF@MnO (typical resulting CV hold times were  $\sim 40$  h). This increased capacity can be attributed to the increased amount of LiF, which, if fully decomposed, can contribute a capacity of  $816 \text{ mAh g}_{\text{MnO}}^{-1}$ . The LiF@MnO from the fully discharged SF<sub>6</sub> cell yielded a much higher lithiation capacity of  $\sim 340 \text{ mAh g}_{\text{MnO}}^{-1}$ , equivalent to  $0.9 \text{ e}^-/\text{MnO}$ , comparable to the highest MnO utilization reported to date.<sup>[8b]</sup> Additional evaluation of the electrochemical behavior difference of ball-milled MnO/LiF and LiF@MnO (from SF<sub>6</sub> and NF<sub>3</sub> discharge) is shown via differential capacity plots in Figure S5. During first charge, the LiF@MnO from the fully or partially discharged Li-SF<sub>6</sub> cells exhibit lower onset potential ( $\sim 4.0$  V) than that of the ball-milled MnO/LiF and NF<sub>3</sub>-formed LiF@MnO ( $\sim 4.2$  V), indicating clearly that the former two cathodes are more favorable for LiF splitting. During discharge, LiF@MnO from NF<sub>3</sub> discharge and partial SF<sub>6</sub> discharge exhibited negligible activity. In contrast, the LiF@MnO from full SF<sub>6</sub> discharge and the ball milled MnO/LiF showed similar profiles with two cathodic peaks, in agreement with that observed in a previous study where two peaks located at 2.5 V and 3.75 V were observed and attributed to Mn redox.<sup>[8b]</sup> Therefore, LiF@MnO from fully discharged SF<sub>6</sub> cells was used in all following experiments.

We next investigated the potential dependence of F<sup>−</sup> incorporation in MnO during the LiF splitting process on first charge in greater detail. LiF@MnO was charged following two additional procedures: CC–CV charge up to 4.7 V, and 4.8 V CC charge without a CV hold. Both charge protocols yielded significantly smaller LiF splitting capacity ( $\sim 300$  vs.  $> 900 \text{ mAh g}_{\text{MnO}}^{-1}$  for a CC–CV charge up to 4.8 V), and only limited capacity ( $\sim 100 \text{ mAh g}_{\text{MnO}}^{-1}$ ) upon subsequent discharge (Figure 4a), indicating insufficient MnO activation. The results reveal that CV charge at 4.8 V is crucial for the activation of bulk MnO to Mn–O–F. This was further confirmed by examination of the bulk Mn valence state by electron energy loss spectroscopy (EELS), focusing on the two charging protocols up to 4.8 V. In Figure 4(b), the Mn L-edge showed negligible change after only CC charge, however, inclusion of the CV step at 4.8 V resulted in a Mn L<sub>3</sub> peak shifted to higher energy (from 640.2 to 641.3 eV), with a significant decrease in the ratio of L<sub>3</sub>/L<sub>2</sub> peak areas, corresponding to oxidization of Mn. Raman spectroscopy was further used to probe the MnO bonding environment change (Figure 4c). The vibrational band at  $645 \text{ cm}^{-1}$  (stretching A<sub>1g</sub> modes of Mn–O bonds in MnO<sub>6</sub> octahedra) and low frequencies ( $< 360 \text{ cm}^{-1}$ , skeletal vibrations) belong to Mn<sub>3</sub>O<sub>4</sub> instead of MnO,<sup>[19]</sup> given that, as was found from previous studies, MnO is easily transformed to Mn<sub>3</sub>O<sub>4</sub> due to beam irradiation during Raman measurements.<sup>[20]</sup> Consistently, the band located at  $645 \text{ cm}^{-1}$  corresponding to the initial MnO phase showed negligible change when CC charged to 4.8 V. In contrast, CV charge resulting in a significant red shift of the Mn–O stretch (to  $\sim 600 \text{ cm}^{-1}$ ) along with the appearance of multiple small-intensity bands at lower frequencies, which cannot be assigned to any single manganese oxide

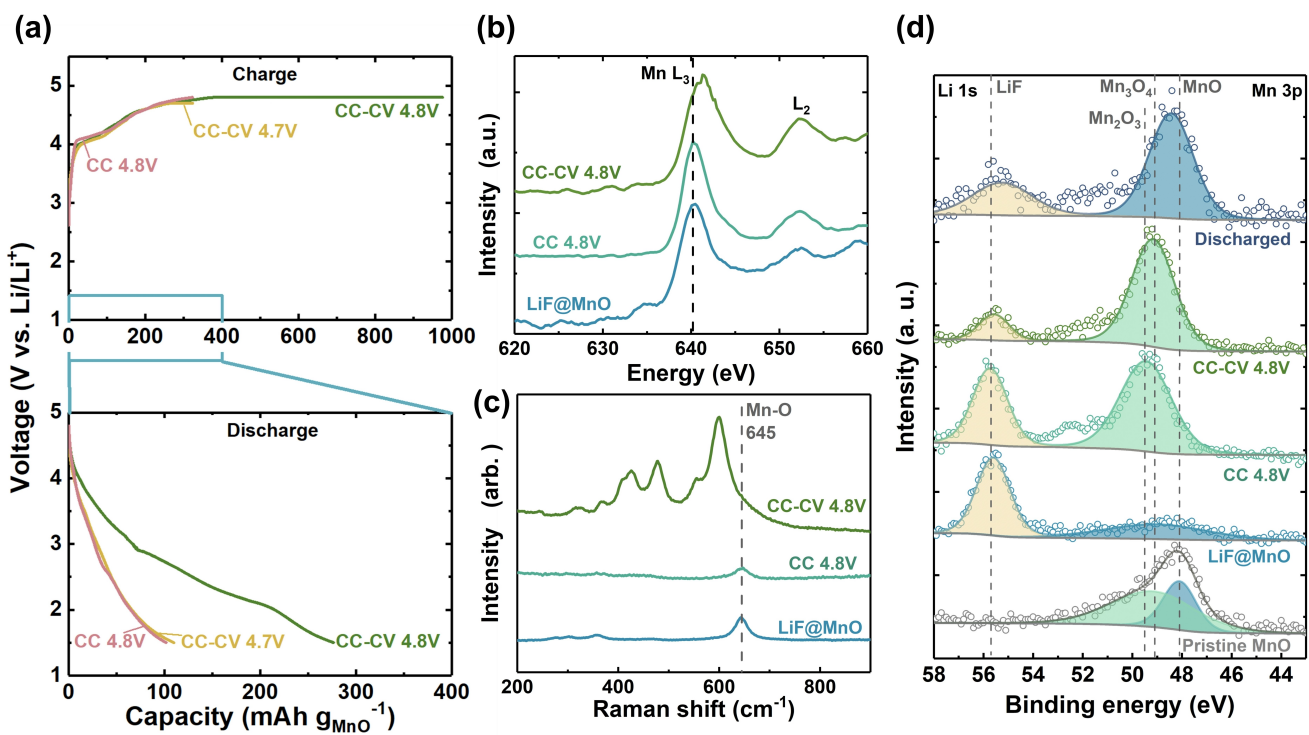


**Figure 4.** a) First charge (LiF splitting) and discharge (lithiation) profiles of LiF@MnO (from fully discharged Li-SF<sub>6</sub> cells; also used for part b–d) at 20 mA g<sub>MnO</sub><sup>-1</sup> with different charge procedures: CC–CV charged to 4.8 V, CC–CV charged to 4.7 V, or CC charged to 4.8 V. Both CV charges were cut off at 10 mA g<sub>MnO</sub><sup>-1</sup>. The lower voltage cutoff upon discharge was 1.5 V. b) EELS of Mn L-edge and c) Raman spectra for LiF@MnO before charge, and after CC or CC–CV charge as indicated. d) High-resolution Li 1s and Mn 3p XPS spectra of the pristine MnO electrode and LiF@MnO at different charge/discharge states. The XPS profile for pristine MnO, CC charged, CC–CV charged, and discharged electrodes are normalized by the Mn 3p peak integrated area. Binding energy reference peaks: LiF 55.7 eV, Mn<sub>2</sub>O<sub>3</sub> 49.5 eV, Mn<sub>3</sub>O<sub>4</sub> 49.1 eV, and MnO 48.1 eV.<sup>[16]</sup> To avoid binder-induced fluoridation, PAN binder was used in the cathode instead of PVDF.

phase.<sup>[21]</sup> The decreased frequency is reflective of the increased Mn–O bond length,<sup>[22]</sup> while the different band positions indicate a more complex Mn bonding environment induced by incorporation of F<sup>−</sup> ions into the MnO lattice, resulting in more defect sites and potential lattice distortion due to the Jahn-Teller effect of Mn<sup>3+</sup>.<sup>[6b]</sup> These findings are consistent with those observed in previous studies on MnO/LiF, where a defective Mn–O–F spinel-like phase was observed after first charge.<sup>[8b,10b]</sup> Notably, such lattice structure change cannot be triggered without LiF: for pristine MnO without LiF coating, negligible change was observed in the Raman spectra after being CC–CV charged to 4.8 V (Figure S6).

The redox process on the MnO surface was also investigated using XPS. From F 1s XPS (Figure S7), the decrease in integrated LiF peak intensity, centered at 684.9 eV, after CV charge is consistent with electrochemical LiF splitting initiation at 4.8 V. The increased contribution from the peak at 686.0 eV, which corresponds to the F<sup>−</sup> ion bonding with the Mn ion,<sup>[8b]</sup> also supports the enhanced depth of LiF splitting and F-incorporation upon CC–CV charge. In addition, Li 1s and Mn 3p, which have closely located binding energies, were examined to provide a clearer observation of the correlated Li and Mn peak evolution (Figure 4d). All spectra are normalized by Mn 3p peak integrated area, except for the uncharged LiF@MnO, in which the Mn signal is strongly blocked by the LiF layer on the surface. After the CC charge, the MnO surface was

oxidized to a phase resembling Mn<sub>3</sub>O<sub>4</sub> (Mn<sup>2+/3+</sup>) or Mn<sub>2</sub>O<sub>3</sub> (Mn<sup>3+</sup>), and retained its oxidation state after further CV charge, suggesting that Mn<sub>3</sub>O<sub>4</sub>/Mn<sub>2</sub>O<sub>3</sub>-like phases precede significant fluoridation. Correspondingly, the Li 1s peak intensity decreased significantly after CV charge, indicating LiF decomposition. Upon subsequent discharge/lithiation, the Li 1s peak recovered and the Mn valence state reverted to be close to Mn<sup>2+</sup>, consistent with reversible redox.

### 2.3. Rate Capability of Mn–O–F Derived from Different Fluorination Sources

We next investigated the attainable rate performance of the first Mn–O–F discharge/lithiation (Figure 5a), with the derived Ragone plot and comparison with other MnO/LiF methodologies shown in Figure 5(b). The MnO utilization (#e<sup>−</sup>/MnO) is calculated based on the discharge/lithiation capacity, with the calculation details described in the supporting information. The highest MnO utilization were achieved at low rate (<30 mA g<sub>MnO</sub><sup>-1</sup>) in all systems. The LiF@MnO (~400 nm) exhibits high MnO utilization (~0.9 e<sup>−</sup>/MnO), comparable to the nano-scale (~8 nm) ball-milled MnO/LiF composites reported previously,<sup>[8b]</sup> and much higher than that of ball-milled MnO/LiF with ~40 nm particle size (<0.7 e<sup>−</sup>/MnO). This indicates that the stringent particle size limitation of MnO in previous studies

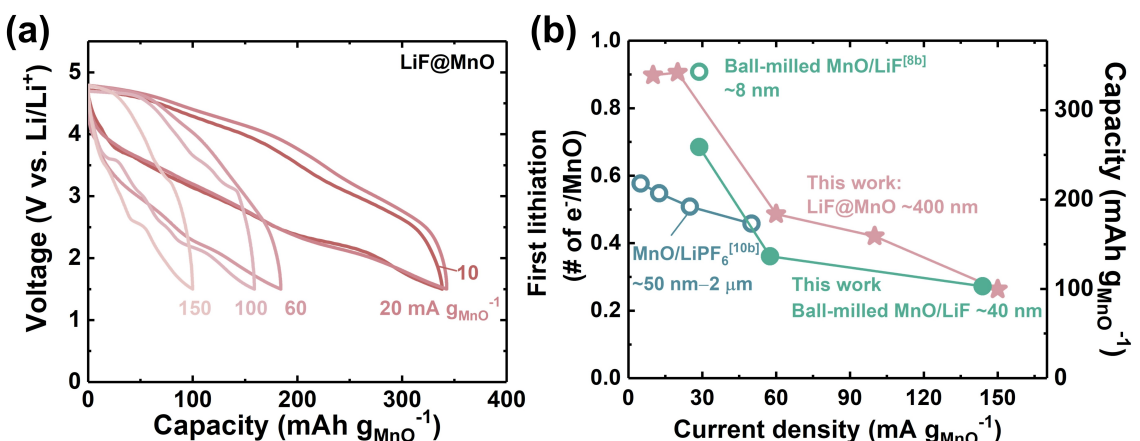


**Figure 5.** a) Rate capability of Mn–O–F. The discharge rates of 10, 20, 60, 100, 150  $\text{mA g}_{\text{MnO}}^{-1}$  correspond to 0.025, 0.05, 0.15, 0.25, and 0.40 C, respectively. The Mn–O–F were derived from LiF@MnO (from fully discharged Li-SF<sub>6</sub> cells; also used for part b) by first CC charge at the corresponding rates to 4.8 V and then CV hold till current drop to half of the initial current. b) Ragone plot comparing the electrochemical performance of LiF–MnO systems as Li-ion cathodes: ball-milled MnO/LiF composite with an average particle size of ~8 nm (data from Ref. [8b]) or ~40 ± 25 nm (synthesized and measured in this study); LiF formed via LiPF<sub>6</sub> decomposition (data from Ref. [10b]); and electrochemically formed LiF@MnO (this study).

is no longer critical when LiF is nano-crystallized and in intimate contact with MnO. In addition, the MnO/LiPF<sub>6</sub> system reported elsewhere, where LiF is formed in situ from LiPF<sub>6</sub> decomposition,<sup>[10b]</sup> used MnO particles with size ~50 nm–2  $\mu\text{m}$ , similar to that of LiF@MnO, but only exhibits ~0.5 e<sup>-</sup>/MnO utilization at ~25  $\text{mA g}_{\text{MnO}}^{-1}$ . As for the rate capability, LiF@MnO demonstrated the highest MnO utilization among all MnO/LiF systems with particle sizes  $\geq$  40 nm. Notably, a relatively steep capacity decrease, from 343  $\text{mAh g}_{\text{MnO}}^{-1}$  to 184  $\text{mAh g}_{\text{MnO}}^{-1}$ , was observed for LiF@MnO as the current density increased from 20  $\text{mA g}_{\text{MnO}}^{-1}$  (~0.05 C) to 60  $\text{mA g}_{\text{MnO}}^{-1}$  (~0.15 C). Further increasing the current density to up to 150  $\text{mA g}_{\text{MnO}}^{-1}$  results in capacity drop to ~100  $\text{mAh g}_{\text{MnO}}^{-1}$ . It is noted that, when cycled at low rates ( $\leq$  20  $\text{mA g}_{\text{MnO}}^{-1}$ ), although the attainable capacities are similar, lowering the current density is helpful for reducing voltage hysteresis of LiF@MnO between charge and discharge (Figure 5a). A similar trend was also observed for ball-milled MnO/LiF prepared in this work, where the capacity decreased from 259  $\text{mAh g}_{\text{MnO}}^{-1}$  to 136  $\text{mAh g}_{\text{MnO}}^{-1}$  as the rate increased to ~60  $\text{mA g}_{\text{MnO}}^{-1}$ , and was comparable to that of LiF@MnO at the highest current density of ~150  $\text{mA g}_{\text{MnO}}^{-1}$ . Therefore, this finding suggests that the conversion reaction between Mn–O–F and MnO–LiF is kinetically limited regardless of the LiF morphology, which may be caused by slow diffusion in the solid phase.

#### 2.4. Trace SF<sub>6</sub> as Additive for Improved Cyclability

When cycled at 20  $\text{mA g}_{\text{MnO}}^{-1}$  (~0.05 C) with 1 M LiClO<sub>4</sub> EC/DMC electrolyte, both LiF@MnO and ball-milled MnO/LiF (~40 ± 25 nm) showed capacity fade from ~340 and 259  $\text{mAh g}_{\text{MnO}}^{-1}$  respectively to ~170  $\text{mAh g}_{\text{MnO}}^{-1}$  after 20 cycles (Figure 6a). The capacity fade can be attributed in part to the severe morphological changes upon repeated lithiation/delithiation and corresponding conversion of Mn–O–F to LiF–MnO, leading

to gradual electronic disconnection and loss of active F for re-incorporation into the parent MnO phase.<sup>[10a]</sup> Therefore, instead of fluorinated salts as used previously to resupply F to the MnO phase,<sup>[10]</sup> we here demonstrate that regulated amounts of dissolved SF<sub>6</sub> (SF<sub>6</sub> solubility in organic solvents: ~2 mM)<sup>[13a]</sup> can function as an effective electrolyte additive and F source. These experiments also allowed examination of the potential for LiF formation and cycling to occur in the same cell, i.e., avoiding the need to change electrolyte to remove residual gas as before. The initial high-capacity LiF formation step was therefore conducted first in a Li-SF<sub>6</sub> cell discharged to full capacity in 1 M LiClO<sub>4</sub> EC/DMC electrolyte (Figure S8), followed by charge activation and direct cycling with an SF<sub>6</sub> gas headspace present. A long discharge plateau (~250  $\text{mAh g}_{\text{MnO}}^{-1}$ ) at ~2.5 V was observed upon subsequent lithiation, the features of which are similar to that observed in Li-SF<sub>6</sub> cells with a characteristic “sudden death” (voltage drop) in the end of discharge (Figure 6b). These features indicate that the discharge activity upon cycling remains governed by SF<sub>6</sub> reduction when there is a large reservoir of SF<sub>6</sub> in the cell. The slightly increased SF<sub>6</sub> discharge potential at ~2.4 V (discharge potential of SF<sub>6</sub> cell at the same rate with pristine MnO/VC is ~2.0 V, Figure S9) is unclear at present, but could be attributed to a cathode morphology change caused by MnO fluoridation. Though good capacity retention (>270  $\text{mAh g}_{\text{MnO}}^{-1}$ ) was attained for the first five cycles, the cell discharge capacity dropped rapidly to ~180  $\text{mAh g}_{\text{MnO}}^{-1}$  by the 9<sup>th</sup> cycle and became unstable (exhibited significant voltage fluctuation) at the 14<sup>th</sup> cycle causing cell termination (Figure 6c). We hypothesize that the instability observed from extended cycling can be attributed to the accumulation of excessive LiF/F<sup>-</sup> in the cathode, which is detrimental given passivating qualities of LiF.

To test this hypothesis and to further improve the cyclability, following the LiF-forming discharge step in 1 M LiClO<sub>4</sub> EC/DMC, cells were then briefly purged with Ar prior to continued cycling to remove excessive SF<sub>6</sub> in the headspace. A

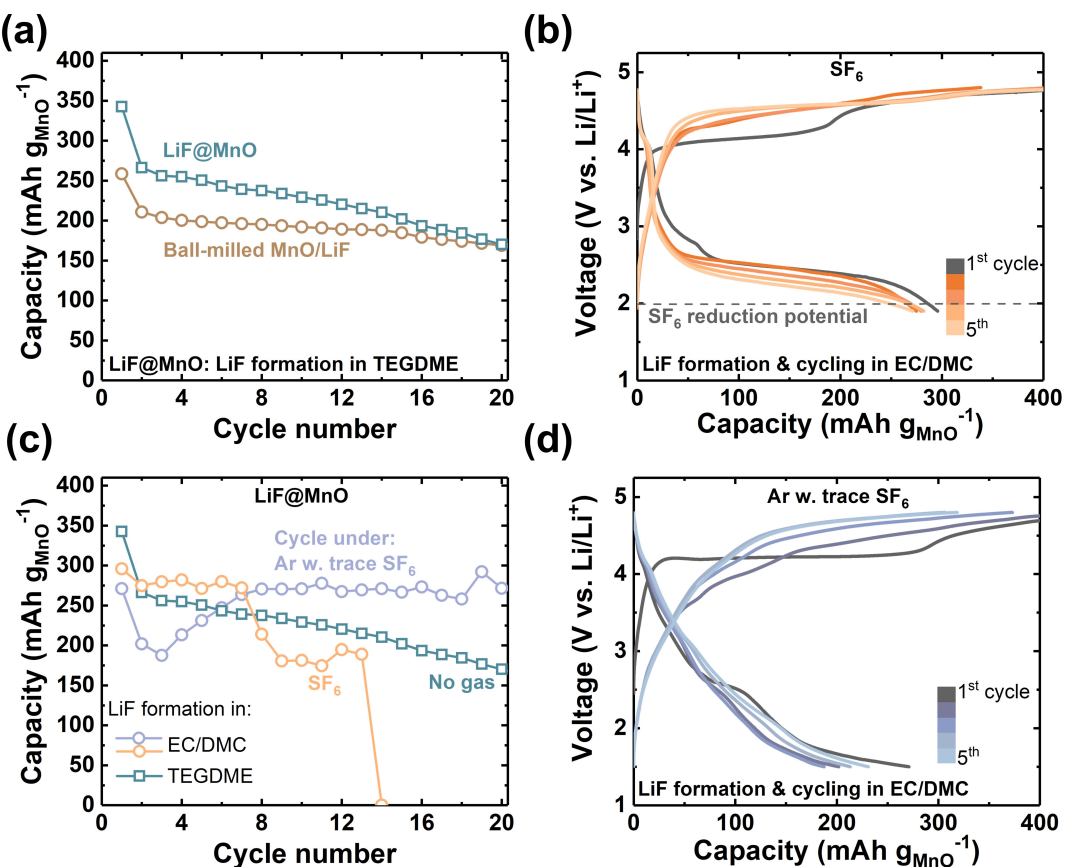


**Figure 6.** a) Discharge capacities as a function of cycle number of ball milled MnO/Li (~40 nm) cathodes and LiF@MnO cathodes (LiF formed from SF<sub>6</sub> discharge in 0.1 M LiClO<sub>4</sub> TEGDME electrolyte). b-d) Electrochemical profiles and cycle performances of LiF@MnO, with LiF formed from SF<sub>6</sub> reduction in 1 M LiClO<sub>4</sub> EC/DMC electrolyte. After LiF formation, b) the cell was directly cycled under SF<sub>6</sub>, or d) purged with Ar, then cycled. c) Discharge capacities as a function of cycle number of LiF@MnO cathodes in part b) and d), compared with the LiF@MnO with LiF formed in TEGDME electrolyte and cycled with no gas present (same data as LiF@MnO in part a). All cells were cycled with 1 M LiClO<sub>4</sub> in EC/DMC electrolyte at 20 mA g<sub>MnO</sub><sup>-1</sup> (~0.05 C).

discharge profile similar to that of LiF@MnO without SF<sub>6</sub> (Figure 3d) is obtained, with the exception of a slightly extended tail at the end of discharge at ~1.5 V (Figure 6d). This is likely caused by the trace amount of SF<sub>6</sub> left in the cell that was not removed by Ar purging due to the high molecular weight of SF<sub>6</sub>. The lower SF<sub>6</sub> reduction voltage than that observed with extra SF<sub>6</sub> present (Figure 6b) can be attributed to the concentration overpotential. Despite the lower capacity (271 mAh g<sub>MnO</sub><sup>-1</sup> vs. 340 mAh g<sub>MnO</sub><sup>-1</sup> for LiF@MnO formed with TEGDME electrolyte) at the beginning of cycling, which might be caused by the solvent-induced LiF crystallinity and particle size difference, this cell exhibits an improved cyclability with capacity higher than 270 mAh g<sub>MnO</sub><sup>-1</sup> retained after 20 cycles (Figure 6c). The detailed mechanism of continued SF<sub>6</sub> reactivity over cycling will be investigated in future studies. However, these findings overall indicate the potential to explore future electroactive F additives to dynamically repair oxide phases as they become F-depleted. In particular, reduction of perfluorinated gases as studied herein occurs well within the electrochemical stability window of the electrolyte, providing a potentially softer fluorination route than those currently reported. The overall fluorination methodology is, however, currently limited by aggressive high voltages and charge

protocols demanded by the intrinsic oxide redox states, which are too high for MnO to likely be feasible for practical cells. We anticipate potential for this methodology of LiF coating and dynamic fluoridation to be adaptable to future oxide substrates with lower oxidation potentials and more complex structures beyond that of the simpler binary phases.

### 3. Conclusions

Activation of the binary oxide MnO to Mn—O—F in the presence of LiF was demonstrated using electrochemically formed LiF grown by the reduction of perfluorinated gas. The small feature size of LiF, which grows directly onto the electronically conductive surfaces of MnO and is therefore in intimate contact with the substrate, allows for effective LiF splitting upon subsequent charge and a high degree of fluoridation, as indicated by high capacities (up to 340 mAh g<sub>MnO</sub><sup>-1</sup>) subsequently accessible upon Li<sup>+</sup> cycling. These capacities correspond to high MnO utilization (~0.9 e<sup>-</sup>/MnO) and are obtained with moderate particle sizes (~400 nm), demonstrating that the stringent particle size requirement for high MnO utilization observed in previous studies (<10 nm) is not necessary as long

as LiF is nano-crystallized and in intimate contact with MnO. The LiF@MnO exhibits improved rate capability compared to other methodologies used to source LiF into a MnO cathode with particle sizes  $\geq 40$  nm. Additionally, SF<sub>6</sub> was shown to be an effective electrolyte additive to support an F-enriched environment near MnO during cycling, leading to stable cycling with capacities  $\sim 270$  mAh g<sub>MnO</sub><sup>-1</sup> at 20 mA g<sub>MnO</sub><sup>-1</sup> over at least 20 cycles. This study indicates that previously reported limits on oxide fluoridation can be overcome by methodologies that allow for improved control over LiF quantity, particle sizes, and overall morphology, which can further contribute to the development of other high-performance cell cathode materials with F substitution (e.g., Li-containing oxides with disordered rock-salt or layered structures) in future work.

## Experimental Section

### Chemicals and Materials

All chemicals, electrodes and cell-making materials were thoroughly dried and stored in an argon-filled glovebox (H<sub>2</sub>O content  $<0.3$  ppm, O<sub>2</sub> content  $<0.3$  ppm, MBRAUN). LiClO<sub>4</sub> (99.99% trace metals basis, Sigma-Aldrich) and the Whatman filter paper (Grade QM-A, 2.2  $\mu$ m pore size, 450  $\mu$ m in thickness, Sigma Aldrich) were dried under active vacuum for 24 hours at 120°C in a Buchi glass oven. TEGDME (99%, Sigma-Aldrich), propylene carbonate (PC, 99.7%, Sigma-Aldrich), EC (99%, Sigma-Aldrich), DMC (>99.9%, Sigma-Aldrich), and MnO (99%, Sigma-Aldrich) were stored inside the glovebox at room temperature.

### Cathode preparation

The as-received MnO particles ( $\sim 0.25$  mm) were combined with Vulcan carbon (VC) (XC-72, Cabot Corporation) (MnO:VC = 7:2 w/w), sealed in the glovebox, and ball-milled by a SPEX ball mill for 3 h. The ball milled MnO/LiF composites were prepared by mixing the MnO with LiF (MnO:LiF = 1:1.2 m/m), as well as VC (20 wt% of total MnO/LiF composite) for 48 h using planetary milling at 400 r.p.m. (Retsch GmbH, Germany). The MnO/VC, and ball-milled MnO/LiF cathodes were fabricated in-house by uniformly coating sonicated inks composed of the as-prepared MnO composites, additional VC, N-Methyl-2-pyrrolidone (NMP), and polyvinylidene difluoride (PVDF) (with a weight ratio of PVDF:VC:MnO composites = 10:20:70) onto a sheet of Toray paper (TGP-H-030, Fuel cell earth). The final weight ratio of PVDF:VC:MnO = 10:35:55. The obtained coated Toray paper was dried at room temperature prior to being punched into circular disks (12 mm diameter), with a typical MnO loading of  $1.12 \pm 0.17$  mg<sub>MnO</sub> cm<sup>-2</sup> (error bar represents five measurements). The MnO cathodes were subsequently dried under active vacuum in a glass oven (Buchi) overnight at 90°C.

### Galvanostatic discharge for LiF formation

Two-electrode Swagelok-type Li-perfluorinated gas cells were constructed in an argon glovebox, with MnO cathode and a 9 mm diameter disk of Li metal as anode (0.75 mm thick, 99.9% metals basis, Alfa Aesar), which was pre-stabilized by soaking in 0.1 M LiClO<sub>4</sub> in PC for more than three days before use.<sup>[23]</sup> The separator (13 mm diameter glass fiber filter paper) was impregnated with 150  $\mu$ L electrolyte solution (0.1 M LiClO<sub>4</sub> in TEGDME). SF<sub>6</sub> (Airgas, 99.999% purity) or NF<sub>3</sub> (Airgas, 99.999% purity) gas was introduced

into cells following their assembly by purging the gas into the cell headspace within the glovebox for approximately 3 min, pressurizing it to  $\sim 1.6$  bar, and then sealing the cell that contains excess amounts of SF<sub>6</sub> or NF<sub>3</sub> gas for subsequent discharge outside the glovebox. The cells were rested at open circuit voltage (OCV) for 15 h before the galvanostatic discharge process, which were carried out (BioLogic VMP3 potentiostat or MPG2 workstation) at the specified current density with a voltage window ranging from OCV to a lower cutoff voltage of 1.6 V vs. Li/Li<sup>+</sup>. The discharged cathodes were extracted from the cell, rinsed with dimethoxyethane (DME), dried and stored inside the glovebox.

### Electrochemical characterization

Two-electrode Swagelok-type Li-ion cells were constructed and sealed in an argon glovebox, with the Li metal as the anode and the pristine/LiF-coated MnO electrode, or ball-milled LiF/MnO electrode (as indicated) as the cathode. The cells were rested at OCV for 5 h and then cycled on a BioLogic VMP3 with 150  $\mu$ L 1 M LiClO<sub>4</sub> in EC/DMC (1:1 v/v) electrolyte impregnated into a glass fiber separator. Unless otherwise indicated, the cells were first constant current (CC) charged to 4.8 V, then constant voltage (CV) charged until the current dropped to half of the current used for CC charge. After the first charge process, the cells were galvanostatically cycled at the same rate as that for the first CC charge between 1.5 and 4.8 V.

### Scanning electron microscopy (SEM)

After charge/discharge, the cell was disassembled inside the glovebox and the cathode was extracted, rinsed with DME, and dried in the argon glovebox prior to SEM characterization. The sample, which was sealed in a glass vial in the glovebox, was then quickly transferred into the SEM chamber for the measurement to minimize the exposure to ambient. All the SEM characterizations were conducted on a Zeiss Merlin High-resolution SEM operating at an accelerating voltage of 5 kV and beam current of 100 pA.

### X-ray diffraction (XRD)

Both pristine and tested/rinsed discharged cathodes were stored inside the glovebox. Prior to XRD measurements, the samples were sealed in an air-sensitive sample holder in the glovebox to minimize atmospheric contamination. XRD patterns were collected on a PANalytical X'Pert Pro multipurpose diffractometer with a copper anode (Cu K<sub>α</sub>). All scans for cathode characterization were performed from  $5^\circ < 2\theta < 90^\circ$  at a typical scan speed of  $0.5^\circ \text{ min}^{-1}$ . Reference data for LiF: space group: Fm 3 m, JCPDS: 00-004-0857.

### Spectroscopic measurements

<sup>19</sup>F Nuclear Magnetic Resonance (NMR) measurements were performed using a Bruker Advance Neo 400 MHz NMR spectrometer. Samples were dissolved in deuterated D<sub>2</sub>O (Sigma-Aldrich) with 2,2,2-trifluoroethanol (TFE, Sigma-Aldrich) as an internal reference. The solutions were then transferred into capped NMR tubes (Wilmad, 528-PP-7) for NMR analysis. Raman spectroscopy was performed on the rinsed charged/discharged cathodes using Renishaw Invia Reflex Micro Raman instrument with a laser excitation wavelength of 785 nm. X-ray photoelectron spectroscopy (XPS) analysis was conducted on a PHI VersaProbe II X-ray Photoelectron Spectrometer. The binding energies were calibrated by the adventitious carbon peak at 284.80 eV. Electron energy loss spectroscopy (EELS) was carried out on a JEOL 2010 FEG analytical

electron microscope equipped with a Gatan image filter for EELS, operating at 200 kV in the parallel beam mode. The samples were quickly transferred into the TEM chamber for the measurement with minimum exposure to ambient.

## Supporting Information

Supporting Information is available from the Wiley Online Library or from the author.

## Acknowledgements

The authors gratefully acknowledge funding from the Army Research Office under award number W911NF-19-1-0311 and from the MIT Energy Initiative Energy Storage Center. This work made use of the MRSEC Shared Experimental Facilities at MIT, supported by the National Science Foundation under award number DMR-14-19807.

## Conflict of Interest

The authors declare no conflict of interest.

**Keywords:** coating • electrochemistry • energy conversion • fluorination • LiF

- [1] a) K. Kang, Y. S. Meng, J. Bréger, C. P. Grey, G. Ceder, *Science* **2006**, *311*, 977; b) M. Armand, J. M. Tarascon, *Nature* **2001**, *414*, 359.
- [2] R. Schmuck, R. Wagner, G. Hörpel, T. Placke, M. Winter, *Nat. Energy* **2018**, *3*, 267.
- [3] P. Rozier, J. M. Tarascon, *J. Electrochem. Soc.* **2015**, *162*, A2490.
- [4] R. Clément, Z. Lun, G. Ceder, *Energy Environ. Sci.* **2020**, *13*, 345.
- [5] a) K. S. Lee, S. T. Myung, K. Amine, H. Yashiro, Y. K. Sun, *J. Electrochem. Soc.* **2007**, *154*, A971; b) J. Yang, L. Xiao, W. He, J. Fan, Z. Chen, X. Ai, H. Yang, Y. Cao, *ACS Appl. Mater. Interfaces* **2016**, *8*, 18867; c) D. H. Seo, J. Lee, A. Urban, R. Malik, S. Kang, G. Ceder, *Nat. Chem.* **2016**, *8*, 692.
- [6] a) A. Windmüller, C.-L. Tsai, S. Möller, M. Balski, Y. J. Sohn, S. Uhlenbrück, O. Guillou, *J. Power Sources* **2017**, *341*, 122; b) Y. Wang, H. T. Gu, J. H. Song, Z. H. Feng, X. B. Zhou, Y. N. Zhou, K. Wang, J. Y. Xie, *J. Phys. Chem. C* **2018**, *122*, 27836; c) S.-H. Kang, K. Amine, *J. Power Sources* **2005**, *146*, 654; d) J. Lee, D. A. Kitchaev, D. H. Kwon, C. W. Lee, J. K. Papp, Y. S. Liu,

Z. Lun, R. J. Clément, T. Shi, B. D. McCloskey, J. Guo, M. Balasubramanian, G. Ceder, *Nature* **2018**, *556*, 185; e) P. Yue, Z. Wang, J. Wang, H. Guo, X. Xiong, X. Li, *Powder Technol.* **2013**, *237*, 623; f) J. K. Ko, K. M. Wiaderek, N. Pereira, T. L. Kinnibrugh, J. R. Kim, P. J. Chupas, K. W. Chapman, G. G. Amatucci, *ACS Appl. Mater. Interfaces* **2014**, *6*, 10858; g) X. Xiong, Z. Wang, X. Yin, H. Guo, X. Li, *Mater. Lett.* **2013**, *110*, 4.

- [7] G. G. Amatucci, N. Pereira, *J. Fluorine Chem.* **2007**, *128*, 243.
- [8] a) N. Dimov, A. Kitajou, H. Hori, E. Kobayashi, S. Okada, *ECS Trans.* **2014**, *58*, 87; b) S. K. Jung, H. Kim, M. G. Cho, S. P. Cho, B. Lee, H. Kim, Y. U. Park, J. Hong, K. Y. Park, G. Yoon, Won M. Seong, Y. Cho, Myoung H. Oh, H. Kim, H. Gwon, I. Hwang, T. Hyeon, W. S. Yoon, K. Kang, *Nat. Energy* **2017**, *2*, 16208; c) S.-K. Jung, I. Hwang, S.-P. Cho, K. Oh, K. Ku, I. R. Choi, K. Kang, *Chem. Mater.* **2018**, *30*, 1956.
- [9] S. K. Jung, I. Hwang, I. R. Choi, G. Yoon, J. H. Park, K. Y. Park, K. Kang, *Adv. Energy Mater.* **2019**, *9*, 1900503.
- [10] a) L. Zhang, G. Chen, E. J. Berg, J. M. Tarascon, *Adv. Energy Mater.* **2017**, *7*, 1602200; b) L. Zhang, D. Dambourret, A. Iadecola, D. Batuk, O. J. Borkiewicz, K. M. Wiaderek, E. Salager, M. Shao, G. Chen, J. M. Tarascon, *Chem. Mater.* **2018**, *30*, 5362.
- [11] a) Y. Zhao, K. Wei, H. Wu, S. Ma, J. Li, Y. Cui, Z. Dong, Y. Cui, C. Li, *ACS Nano* **2019**, *13*, 2490; b) K. Wei, Y. Zhao, K. Chen, K. Sun, T. Wu, Z. Dong, Y. Cui, C. Zeng, C. Li, *Adv. Funct. Mater.* **2021**, 2009133.
- [12] F. Jiang, P. Peng, *Sci. Rep.* **2016**, *6*, 1.
- [13] a) Y. Li, A. Khurram, B. M. Gallant, *J. Phys. Chem. C* **2018**, *122*, 7128; b) H. Gao, Y. Li, R. Guo, B. M. Gallant, *Adv. Energy Mater.* **2019**, 1900393.
- [14] M. He, Y. Li, R. Guo, B. M. Gallant, *J. Phys. Chem. Lett.* **2018**, *9*, 4700.
- [15] P. Poizot, S. Laruelle, S. Grangeon, L. Dupont, J. Tarascon, *Nature* **2000**, *407*, 496.
- [16] NIST X-ray Photoelectron Spectroscopy Database, NIST Standard Reference Database Number 20, National Institute of Standards and Technology, Gaithersburg MD, 20899 (2000), doi:10.18434/T4T88 K.
- [17] SDBSWeb: <https://sdbs.db.aist.go.jp> (National Institute of Advanced Industrial Science and Technology).
- [18] a) M. M. Ottakam Thotiyl, S. A. Freunberger, Z. Peng, P. G. Bruce, *J. Am. Chem. Soc.* **2012**, *135*, 494; b) R. Imhof, P. Novák, *J. Electrochem. Soc.* **1999**, *146*, 1702.
- [19] S. Bernardini, F. Bellatreccia, A. Casanova Municchia, G. Della Ventura, A. Sodo, *J. Raman Spectrosc.* **2019**, *50*, 873.
- [20] a) Y. Mai, D. Zhang, Y. Qiao, C. Gu, X. Wang, J. Tu, *J. Power Sources* **2012**, *216*, 201; b) I. Rusakova, T. Ould-Ely, C. Hofmann, D. Prieto-Centurión, C. S. Levin, N. J. Halas, A. Lütgge, K. H. Whitmire, *Chem. Mater.* **2007**, *19*, 1369; c) X. Li, Y. Zhu, X. Zhang, J. Liang, Y. Qian, *RSC Adv.* **2013**, *3*, 10001.
- [21] D. T. Zahn, *Phys. Chem. Chem. Phys.* **1999**, *1*, 185.
- [22] C. Julien, M. Massot, C. Poinsignon, *Spectrochim. Acta Part A* **2004**, *60*, 689.
- [23] Z. Peng, S. A. Freunberger, Y. Chen, P. G. Bruce, *Science* **2012**, *337*, 563.

Manuscript received: June 23, 2021

Revised manuscript received: August 1, 2021

Accepted manuscript online: August 21, 2021

Version of record online: September 3, 2021